Solution of the Noh problem with an arbitrary equation of state

A. L. Velikovich and J. L. Giuliani

Plasma Physics Division, Naval Research Laboratory, Washington, DC 20375, USA

The classic self-similar solutions of the nonstationary compressible Euler equations obtained for a blast-wave propagation (Sedov, Taylor, and von Neumann), a shock-wave implosion (Guderley, Landau, and Stanyukovich), or an impulsive loading of a planar target (von Hoerner, Häfele, and Zel'dovich) have all been derived for a polytropic ideal gas. None of them can be generalized for a fluid with an arbitrary equation of state (EOS), such as the van der Waals EOS of a non-ideal-gas or a three-term EOS of a condensed material. We demonstrate here that the Noh accretion-shock problem is an exception. Its self-similar solutions exist in cylindrical and spherical geometry for fluids and materials with an arbitrary EOS. Such solutions for finite accretion-shock strength and nonuniform inflow velocity are constructed semianalytically with a model three-term equation of state that includes cold, thermal ion (lattice), and thermal electron contributions to the pressure and internal energy. Examples are presented for aluminum and copper. Other material- and EOS-specific semianalytic solutions of the Noh problem can be easily constructed using the same method for any material that in the pressure range of interest can be approximated as a dissipation-free fluid with an arbitrary equation of state.

I. INTRODUCTION

The classic Noh self-similar solution [1] describes a supersonic stagnation of a cold ideal gas streaming to the plane, center, or axis of symmetry in a strong accretion shock wave. The hydrodynamic flow modeled by this solution plays an important role in a wide range of physical phenomena, from astrophysics to high-energy-density physics (HEDP) and inertial confinement fusion (ICF).

Spherical accretion shock fronts separating a cold infalling gas from the hot shocked plasma are encountered in a variety of astrophysical objects, from white dwarfs to core-collapse supernovae; see [2,3] and references therein. Stagnation and shock heating of accelerated converging plasmas take place in many HEDP and ICF experiments. In laser-driven ICF, spherical stagnation constitutes the first stage of the hot spot formation, between the implosion of the leading shock wave in the fuel vapor at the target center and the moment when the shock wave reflected from the center reaches the converging dense DT shell. In cylindrical wire-array Z-pinch implosions, an almost uniform, low-density, cold precursor plasma coasts to the pinch axis, stagnating via an expanding accretion shock wave into a fairly stable precursor plasma column; see [4–6] and references therein. The kinetic-to-thermal energy conversion via an expanding cylindrical accretion shock wave has been demonstrated to play a major role in the keV x-ray radiation production in both gas-puff and wire-array Z pinches [7]. The same applies to the deuterium gas-puff Z-pinch implosions on the Z facility that produced large yields of DD fusion neutrons [8]. The classic Noh solution and its generalizations, both in hydrodynamics [6,9] and in MHD [10], provide convenient tools for a simple theoretical analysis of these phenomena. These solutions also help get an insight into the complicated 3D behavior of wire-array Z-pinch plasmas [6] and make simple theoretical estimates of neutron yields

in spherical implosions of laser targets [11] and cylindrical implosions of Z-pinch plasmas [6,8,12].

Simplicity of the Noh problem formulation and of its explicit solution made it the workhorse of compressible hydrocode verification for over three decades. This deceptively simple benchmarking test problem "poses a formidable challenge to all hydrodynamics codes since they have to deal with an infinitely strong shock" [9], and is able "to dramatically reflect any underlying numerical solver pathologies (e.g., asymmetries and wall-heating phenomena)" [13]. References [14–35] are a small selection from the vast body of literature on numerical methods in astrophysics and physics of fluids and plasmas, where the classic Noh solution has been used as an indispensable test problem. There is increased interest in utilizing such test problems to simulate turbulent flows induced by the Richtmyer-Meshkov (RM) instability [36,37]; see the reviews [38,39] and references therein.

Indeed, a deep connection can be traced between the physical picture of stagnation as modeled by the classic Noh solution and the RM instability. In our recent paper containing the perturbation analysis of the classic Noh solution [40], we discussed the analogy between the spectra of the perturbed Noh flow and that of an RM-unstable flow in planar geometry; see Sec. III B of Ref. [41]. In both cases, the main manifestation of the compressibility of the shocked material is the reverberation of the sonic waves between transmitted shock front(s) and either the unstable material interface, in the case of the RM instability in planar geometry, or the axis or center of symmetry, in the case of the classic Noh accretion-shock flow in cylindrical and spherical geometries, respectively. The eigenvalues for all the stable sonic modes are almost identical, with an obvious correction accounting for the difference between cylindrical or spherical geometries of the classic Noh solution, and planar geometry of the RM-unstable flow. But the latter has also another eigenmode, which

013105-1

is localized at the perturbed material interface and describes the small-amplitude RM perturbation growth. The classic Noh accretion-shock flow does not involve a free surface or a material interface, where an RM or Rayleigh-Taylor instability could develop. Hence, all of its eigenmodes are stable [40]. This is one of the reasons why it is such an important test problem.

The classic Noh solution has been constructed for a fluid that is dissipationless (no viscosity, no thermal conduction) and has an ideal-gas equation of state (EOS): $p = \rho T/m_a$, $\varepsilon = p/[\rho(\gamma - 1)]$, where p, ρ, T, and ε are the pressure, density, temperature (in energy units), and specific energy of the gas, respectively, the constant $\gamma > 1$ is the adiabatic exponent, and m_a is the atom mass. Exploring the process of stagnation, one encounters a number of interesting problems involving physics that are not accounted for in the classic Noh solution. For example, how well does the one-dimensional (1D) classic Noh solution describe two- or three-dimensional (2D or 3D) stagnation? How is the stagnating flow modified if the converging fluid is dissipationless but its EOS is not ideal-gas? These questions are obviously interrelated. If the EOS of the converging fluid does not satisfy the stability conditions formulated in [42–44], the instability of a shock front can certainly affect the stability of the solution as a whole. Alternatively, the 1D stagnation of a material with an EOS that is "nonconvex" (which means that it does not have the "normal thermodynamic properties" as defined in Chap. I, Sec. 17, of Ref. [45]: the derivative $[\partial^2(1/\rho)/\partial p^2]_S$ along the isentrope is not positive-definite) can proceed via a rarefaction accretion wave rather than a shock front.

In recent years, significant progress has been made towards answering both of the above questions. First, the generalized Noh solutions for the non-ideal-gas EOS satisfying certain symmetry conditions outlined in Ref. [46] have been obtained [13,47]. Numerical study of the RM instability in planar geometry had been reported for a Mie-Grüneisen equation of state [48]. In this case, the 1D background flow is a solution of a planar Riemann problem of shock-interface interaction, quite similar to the simple particular case of a rigid piston problem defining the planar Noh accretion-shock solution. Second, the physical stability of the classic Noh solution has been proven [40]. The long experience of successful verification of the 2D and 3D hydrocodes with the classic Noh solution is an indication, although not a proof, that the latter is physically stable: the small perturbations introduced by the discrete grid do not make the stagnating flow deviate from the self-similarity and one-dimensionality. A deviation of the simulated solution from the analytic one, such as shown in Fig. 21 of [32], indicates problems with the code. In Ref. [40], we have demonstrated that the physical stability of the classic Noh solution is ensured by the stability of a shock front in an ideal gas. In other words, the Noh accretion-shock flow is stable because the reflection coefficient for the sound waves incident upon the expanding shock front from the shocked gas is less than unity for an ideal gas with an arbitrary γ. The stable classic Noh solution is therefore an attractor, asymptotically approached by the 3D solutions close to it. This conclusion can change if this reflection coefficient is greater than unity, or even diverges, which means that an isolated shock front itself can generate sonic waves, as happens in fluids whose EOS satisfies

the conditions for the D'yakov-Kontorovich (DK) instability [42–44]. It is not known yet how this instability will affect the accretion-shock flow. For a planar version of a generalized Noh accretion-shock solution, such analysis has been done in two recent publications [49,50] whose results are not in agreement.

A self-similar solution generalizing the classic Noh solution for an arbitrary EOS, not necessarily satisfying the symmetry constraints [13,46,47], would make a convenient platform for a theoretical study of the stability of externally driven expanding shock fronts in spherical and cylindrical geometry. Generation of new, multidimensional, semianalytic verification solutions capable of testing the accuracy of 2D and 3D modeling of small perturbation evolution in shocked fluids would be an additional benefit of such study. Such solutions would enable code verification in both stable and unstable conditions, taking into account finite shock strength and the EOS specifics. The generalized Noh solutions for an arbitrary EOS have not been derived so far, and in the literature one can find statements that it cannot be done at all. Below we demonstrate how this problem is solved.

This paper is structured as follows. In Sec. II, we describe the formulation of our problem. In Sec. III, we introduce a model three-term EOS [45] based on the simple analytical form of the density-dependent Grüneisen coefficient suggested in Refs. [51,52]. This EOS does not satisfy the constraints formulated in Refs. [13,46,47]. In Sec. IV, we construct examples of semianalytic self-similar solutions of the Noh problem with this EOS in cylindrical and spherical geometry for aluminum and copper. We demonstrate how these solutions converge to the strong-shock solutions described in Ref. [47] in the high-pressure range. In Sec. V, we conclude with a discussion.

II. FORMULATION OF THE PROBLEM

The general Noh problem is formulated as follows. At $t = 0^-$, an infinite space is filled with a uniform material whose density is denoted by ρ_0. Its initial velocity is supersonic, it has the same absolute value u_0 everywhere, and it is directed at each point to the plane, axis, or center of symmetry in the cases of planar, cylindrical, or spherical symmetry, respectively. The 1D accretion-shock flow emerging after $t = 0^+$ maintains its initial planar, cylindrical, or spherical symmetry. We need to determine the preshock profiles of density, pressure, and velocity and calculate the strength of the expanding shock wave and the postshock conditions.

The Noh problem belongs to the family of the fundamental 1D problems of compressible fluid dynamics that involve shock waves and permit self-similar solutions, such as the Sedov–Taylor–von Neumann blast-wave problem [46,53], the converging-shock problem independently solved by Guderley [54] and Landau and Stanyukovich [55], and the problem of gas motion under the action of an impulsive load studied by von Hoerner, Häfele, Zel'dovich, and other authors [45,56]. In this large family, the Noh problem stands out for several reasons, one of them being the utmost simplicity of its classic solution. If the material is an ideal gas initially at zero temperature and pressure, then this problem has an explicit self-similar solution [1]. The accretion shock wave expands from the plane, center, or axis of symmetry at the constant velocity $u_s = u_0/(R_C - 1)$,

where R_C is the density compression ratio in the expanding shock wave. For an ideal gas in the strong-shock limit $R_C = (\gamma + 1)/(\gamma - 1)$. The shocked gas is at rest, and its density and pressure are uniform and given by

$$\rho(r, t) = \rho_s = R_C^m \rho_0, \; p(r, t) = p_s = \frac{1}{R_C - 1} \rho_s u_0^2, \quad r \leqslant u_s t,$$
(1)

where the values of the geometric parameter $m = 1$, 2, and 3 refer to the planar, cylindrical, and spherical geometry, respectively. The preshock profiles of the density, pressure, and radial velocity are

$$\rho(r, t) = \left[1 + (R_C - 1) \frac{u_s t}{r} \right]^{m-1} \rho_0,$$

$$p(r, t) = 0, \quad u(r, t) = -u_0, \quad r > u_s t.$$
(2)

The preshock density buildup in (2) for the cylindrical and spherical geometry is due to the convergence of the incident gas flow. The assumption of zero initial pressure combined with the ideal-gas EOS ensures that there is no corresponding pressure buildup, and therefore the velocity of the convergent gas remains constant, equal to u_0. The shock velocity with respect to the incident material is therefore

$$D = u_0 + u_s = \frac{R_C}{R_C - 1} u_0 = R_C u_s.$$
(3)

For the spherical and cylindrical geometry, $m = 2$ and 3, the accretion-shock stagnating flow described by the classic Noh solution involves adiabatic compression of the converging gas (2) followed by its shock compression. For the case of planar geometry, $m = 1$, which involves no convergence, and hence, no adiabatic compression, the Noh problem reduces to the rigid piston problem, a particular case of the planar Riemann problem, the evolution of a step-function discontinuity in the initial conditions; see Sec. 100 of [44]. Obviously, the solution of this problem, which includes pre- and postshock areas of uniform flow separated by a shock front, can be obtained for an arbitrary EOS [13,48–50], and we will not discuss this case below.

Over the years, the interest in the Noh problem has stimulated a few generalizations of its original formulation. For example, the piston problem involving multiple shock reflections from the piston and the plane, center, or axis of symmetry has been studied in Ref. [9]. Most of the generalized solutions are semianalytic, that is, not given by explicit analytic formulas but rather obtained with the aid of numerical integration of ordinary differential equations, exactly as is the case for the classic converging-shock solutions [54,55]. For example, semianalytic self-similar solutions have been obtained for the cases when the density and/or velocity profiles at $t = 0^-$ are not flat [6] and for the magnetohydrodynamic Noh problem [10].

In this article, we describe another possible generalization of the Noh solution that involves a non-ideal-gas equation of state of the converging material. The issue of compatibility of the self-similar solutions of the compressible Euler equations with a non-ideal-gas EOS was first analyzed by Sedov [46]. He used dimensional analysis to demonstrate that the blast-wave problem has a self-similar solution if the specific internal energy $\varepsilon(p, \rho)$ is proportional to the pressure p with a coefficient

that depends only on the density ρ. The EOS satisfying this requirement can be presented in the Mie-Grüneisen form as

$$p = \Gamma(\rho) \rho \varepsilon,$$
(4)

where $\Gamma(\rho)$ is a density-dependent Grüneisen coefficient. The ideal-gas EOS is obviously a particular case of Eq. (4) with $\Gamma(\rho) = \gamma - 1 = \text{constant}$. Although Eq. (4) contains an arbitrary function of density, it is not a general form of an equation of state. For example, the van der Waals EOS cannot be presented in this form [46]. Sedov's conclusion based on the dimensional analysis is also applicable to the solutions of the converging-shock problem [54,55] and the impulsive-loading problem [45,56], where the self-similarity is not derived from the dimensional considerations; see the discussion in Chap. XII of Ref. [45]. A self-similar solution of the impulsive-loading problem with the Mie-Grüneisen EOS (4) is presented in Ref. [57]. Self-similar solutions of the Guderley converging-shock problem have been published for the "reduced" van der Waals [58] and Mie-Grüneisen [59] EOS.

The study of the Noh problem with the aid of the Lie symmetries theory [13,47] resulted in the constraints on the EOS similar to those formulated by Sedov [46]. One of the examples of an equation of state satisfying these constraints in [47] is the Mie-Grüneisen EOS (4). Under the assumption that the specific internal energy, pressure, and speed of sound in the converging preshock material are zero, the solution (1) and (2) was reproduced [47], with the strong-shock value of $R_C = 1 + 2/\Gamma_2$, the subscript 2 indicating the value of the density-dependent Grüneisen coefficient immediately behind the expanding shock front. By the same token, it has recently been demonstrated in Ref. [13] that if the adiabatic bulk modulus of the preshock material cannot be neglected, then the constant-velocity solution (2) does not exist for cylindrical and spherical geometry. Physically, this means that when an adiabatic density compression is accompanied by a pressure buildup, the velocity profile of the converging preshock material in cylindrical and spherical geometry cannot remain flat. Hence the conclusion made in Ref. [13]: in a medium with an EOS that accounts for the cold energy, the Noh problem has a self-similar solution with a constant inflow velocity only for a planar geometry, in which case it reduces to a simple particular case of the Riemann problem, as discussed above.

Our formulation of the generalized Noh problem does not include the assumption of uniform inflow velocity, $u = \text{constant} = u_0$, which is assumed in [13] to be inherent to the Noh problem definition. This constraint is actually in addition to the aim of finding a self-similar solution. Here we demonstrate that cylindrical and spherical self-similar solutions of the Noh problem with nonuniform inflow velocity exist for dissipationless fluids with arbitrary EOS. In other words, the existence of such self-similar solutions requires only that the fluid is dissipationless, and does not impose any constraints on its EOS, like those derived in Refs. [46,47]. For these solutions, the density gradient produced by the adiabatic compression of the converging preshock material translates into a finite pressure gradient, which is consistent with any EOS approximating the behavior of an adiabatically compressed condensed material. The pressure gradient, in turn, slows down the incident material, so that the velocity of the

material entering the expanding shock front is less than u_0. The density and pressure of the resting shocked material are still uniform but they are not given by Eq. (1). Rather, they have to be determined self-consistently in the process of the problem solution.

III. A MODEL THREE-TERM EOS

We will demonstrate the existence of self-similar solutions of the Noh problem in cylindrical and spherical geometry using a version of the three-term equation of state described in Chap. XI, Sec. 6, of Ref. [45]. This form of the EOS can provide a satisfactory description of adiabatic and shock compression of condensed materials in the pressure range up to several Mbar:

$$\varepsilon(\rho, T) = \varepsilon_c(\rho) + \varepsilon_T(\rho, T) + \varepsilon_e(\rho, T), \tag{5}$$

$$p(\rho, T) = p_c(\rho) + p_T(\rho, T) + p_e(\rho, T). \tag{6}$$

Here, the cold, or elastic, terms, ε_c and p_c, are related to the forces of interaction between the atoms of the material at $T = 0$, and therefore they depend only on the material density ρ. The thermal ion (lattice) terms, ε_T and p_T, as well as the thermal electron terms, ε_e and p_e, are functions of both density and temperature. By excluding the temperature variable, one can present the EOS (5), (6) in the form $\varepsilon = \varepsilon(p, \rho)$ and check that it does not satisfy the general symmetry criteria, such as Eq. (11.28) of Ref. [46] or Eq. (50) of Ref. [47], that allow the existence of self-similar solutions of the blast-wave, imploding-shock, and impulsive-loading problems. Note that the convenient decomposition (5), (6), which is often used to construct tabular equations of state [60], cannot be derived from first principles because the motions of the free and bound electrons and ions in a real fluid are all coupled. In Ref. [61], a discussion of the validity of the assumptions underlying the model (5), (6) is found.

To construct numerical examples of the self-similar solutions of the cylindrical and spherical Noh problem sought, we need to specify the functions entering Eqs. (5), (6). Below, we use a particularly simple form of Eqs. (5), (6) as an analytically treatable example of an EOS, in which the relation between p and ε is not "separable and homogeneous" [59], and which thereby does not satisfy the symmetry requirements of [46,47]. As discussed below, our simple model EOS does not provide an accurate approximation of the real equations of state for aluminum and copper, and there are many ways of improving its accuracy. But the self-similar solutions of the generalized Noh problem could be readily constructed in the same way for other, more accurate analytic EOSs, including those which are not based on the decomposition (5), (6) [61].

We use the one-parameter approximation of the cold curve due to Molodets [51,52]. The density dependence of the Grüneisen coefficient on the isotherm $T = 0$ is heuristically postulated in the form

$$\Gamma(\rho) = \frac{2}{3} + \frac{2}{a(\rho/\rho_{0a}) - 1}. \tag{7}$$

Here, ρ_{0a} is the density of the material at zero temperature and zero pressure, $T = 0$ and $p = 0$. The density ρ_{0a} is higher
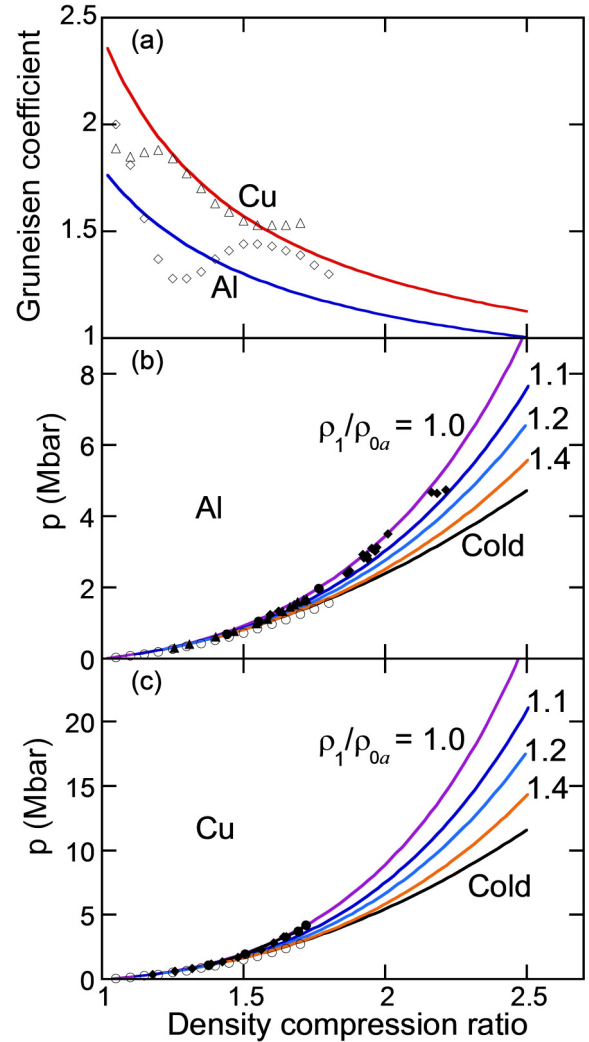

FIG. 1. (a) Grüneisen coefficient vs density compression as given by Eq. (7) for Al and Cu (lines) and inferred experimental values (diamonds for Al, triangles for Cu) from Ref. [62]. (b) and (c) Cold compression curve and Hugoniot curves for Al and Cu, respectively, starting from the zero-temperature isotherm-isentrope, the preshock density being $\rho_1/\rho_{0a} = 1$, 1.1, 1.2, and 1.4. Empty circles represent the cold compression curve calculations from Ref. [62]. Solid circles, triangles, and diamonds represent the experimental data for the principal Hugoniots of aluminum and copper taken from Refs. [62,72], and [73] (Al only), respectively.

than the normal density ρ_0 of the same material because of the thermal expansion that stretches the lattice, producing a negative cold pressure at room temperature. For example, in Al this negative pressure at room temperature [45] is about -17 kbar, which is compensated by an almost equal positive thermal contribution to make the total pressure 1 bar or zero, which makes little difference. The value of the Grüneisen coefficient at the density ρ_{0a} is denoted by Γ_{0a}, and the dimensionless parameter of the theory a is evaluated from (7): $a = 1 + 2/(\Gamma_{0a} - 2/3)$. Figure 1(a) compares the density dependence of the Grüneisen coefficient (7), with the parameters listed in Table I for aluminum and copper [52], to the values inferred from the experimental data of Ref. [62] (symbols). The monotonic lines (7) are seen to reproduce the

TABLE I. Equation-of-state constants [51,52] for Al and Cu and parameters of the Noh solutions illustrated in Figs. 2 and 3.

	Al				Cu	
ρ_{0a} (g/cm^3)	2.789414				9.075238	
ρ_0 (g/cm^3)	2.73				8.93	
Γ_{0a}	1.798175				2.421139	
a	2.767552				2.139944	
K_{0a} (GPa)	91.133				146.16	
β_0 (ergs/g K)	500				110	
Geometry	Cylindrical		Spherical		Cylindrical	
Shock strength	Weak shock	Strong shock	Weak shock	Strong shock	Weak shock	Strong shock
v_s (km/s)	10	15	15	20	10	50
v_0 (km/s)	5.336	22.89	10.10	25.82	7.416	142.4
D (km/s)	14.03	35.94	21.00	39.62	16.04	191.7
ρ_1/ρ_{0a}	1.611	2.609	3.024	5.640	1.782	3.857
$\rho_2/\rho_1 = R_C$	1.403	2.396	1.400	1.981	1.604	3.834
ρ_2/ρ_{0a}	2.259	6.250	4.233	11.17	2.859	14.79
p_1 (Mbar)	1.098	5.329	7.948	34.68	3.514	39.70
p_2 (Mbar)	3.637	60.08	18.57	157.0	19.18	9549
T_2 (eV)	0.1759	7.286	0.3243	5.519	1.314	263.4

general trends of the experimental curves $\Gamma(\rho)$, although the fine details are not captured.

The cold pressure as a function of density is found by substituting (7) into the left-hand side of the Landau-Slater formula [45,63,64],

$$\Gamma(\rho) = \frac{\rho}{2}\frac{\frac{d^2 p_c}{d\rho^2}}{\frac{d p_c}{d\rho}} + \frac{1}{3}, \quad (8)$$

and integrating the resulting differential equation. Denoting the normalized density by $z = \rho/\rho_{0a}$, we present the result of the first integration in the form

$$\frac{d p_c}{d\rho} = \frac{K_{0a}(az-1)^4}{\rho_{0a}(a-1)^4 z^{10/3}}, \quad (9)$$

where K_{0a} is the value of the adiabatic bulk modulus $K = \rho(\partial p/\partial\rho)_S$ extrapolated in [51,52] to $T = 0$ and $\rho = \rho_{0a}$ as a fitting parameter of the theory. Integrating (9) with the boundary condition $p_c(\rho_{0a}) = p_c(z=1) = 0$, we obtain [51,52]

$$p_c = \frac{3K_{0a}}{(a-1)^4}\left(\frac{1}{5}a^4 z^{5/3} - 2a^3 z^{2/3} - 6a^2 z^{-1/3} + az^{-4/3}\right.$$
$$\left. -\frac{1}{7}z^{-7/3} - \frac{1}{5}a^4 + 2a^3 + 6a^2 - a + \frac{1}{7}\right). \quad (10)$$

Substituting (10) into the definition of the cold energy, $p_c = \rho^2 d\varepsilon_c/d\rho$, and integrating the resulting equation with the boundary condition $\varepsilon_c(\rho_{0a}) = 0$, we find [51,52]

$$\varepsilon_c = \frac{3K_{0a}}{(a-1)^4\rho_{0a}}\left(\frac{3}{10}a^4 z^{2/3} + 6a^3 z^{-1/3}\right.$$
$$+ \frac{7a^4 - 70a^3 - 210a^2 + 35a - 5}{35}z^{-1}$$
$$+ \frac{9}{2}a^2 z^{-4/3} - \frac{3}{7}az^{-7/3} + \frac{3}{70}z^{-10/3}$$
$$\left. -\frac{1}{2}a^4 - 4a^3 + \frac{3}{2}a^2 - \frac{4}{7}a + \frac{1}{10}\right). \quad (11)$$

These simple formulas yield reasonably accurate cold compression curves for numerous solid materials; see Refs. [51,52,65,66] and references therein. The zero-temperature isotherms-isentropes (10) are shown as lines labeled "Cold" in Figs. 1(b), 1(c) for aluminum and copper, respectively. The cold compression curves inferred from the experimental data [62] for the same materials are also shown with empty circle symbols. They are seen to be in fair agreement with the prediction of the Molodets model.

An analytic approximation of the relation between the Grüneisen coefficient and the cold pressure different from (8) is due to Dugdale and MacDonald [67]; it had been used for the analysis of the Hugoniot data in Ref. [62] and in many subsequent publications. When the Dugdale-MacDonald approximation is used, Eqs. (10) and (11) must be replaced by the formulas found in Ref. [66].

We use the simplest approximation of the ion (lattice) thermal contributions to the specific internal energy and pressure:

$$\varepsilon_T = \frac{3}{m_a}T, \quad (12)$$

$$p_T = \Gamma\rho\varepsilon_T = \frac{3\rho_{0a}}{m_a}z\Gamma(z)T, \quad (13)$$

where the temperature is expressed in energy units. It is possible [51,52,65,66] to account for the temperature correction to the Grüneisen coefficient. One can take into account the nonharmonic corrections to ε_T and p_T calculated for a one-component plasma by the Monte Carlo method [68], thereby generalizing the Mie-Grüneisen model, but below we will not use these corrections.

The electronic contributions to the specific internal energy and pressure can be presented as [45,66]

$$\varepsilon_e = \frac{1}{2}\beta_0 z^{-\Gamma_e}T^2, \quad (14)$$

$$p_e = \frac{\Gamma_e}{2}\beta_0\rho_{0a}z^{1-\Gamma_e}T^2, \quad (15)$$

where Γ_e is the electronic Grüneisen coefficient. The T^2 dependence is a reasonable approximation for postshock temperatures much lower than the Fermi energy of the electron gas, and hence, for a limited shock strength. If we choose [45,66] a constant value of $\Gamma_e = 2/3$, then the density and temperature dependence of ε_e and p_e in (14), (15) would exactly correspond to a free electron gas at a temperature well below the Fermi energy. The constant β_0 is then determined by the number of free electrons per unit mass of the material at $T = 0$ and $\rho = \rho_{0a}$; cf. Eq. (11.24) of Ref. [45]. The constant value of $\Gamma_e = 2/3$ in Eqs. (14), (15) reflects the assumption that this number does not change with the shock strength, which, of course, cannot be rigorously justified. The experimental data [45,62] indicate that the value of $\Gamma_e = 1/2$ is a better approximation for simple metals at postshock temperatures between 3 and 5 eV. In the multi-Mbar pressure range, the number of free electrons is determined by the consecutive ionization of atomic shells [69], which leads to a very different temperature dependence of the electronic contributions [68]. In tabular EOSs, the electronic terms are typically evaluated using the quantum average-atom model [70,71]. Since our purpose is to present examples of self-similar solutions for an EOS free of the previously formulated constraints, rather than to derive an accurate analytical EOS model, below we will use the simplest form of Eqs. (14), (15) with $\Gamma_e = 2/3$.

The Hugoniot equations we are interested in describe shock transitions from the cold isotherm-isentrope $T = 0$. The cold material can be isentropically compressed to a higher density than ρ_{0a}. The preshock cold state labeled by the subscript 1 is fully determined by the normalized density, $\rho_1 = \rho_{0a} z_1$, where $z_1 \geqslant 1$. The corresponding values of the preshock specific internal energy and pressure, $\varepsilon_1 = \varepsilon_c(z_1)$ and $p_1 = p_c(z_1)$, are given by Eqs. (11) and (10), respectively. The postshock state labeled by the subscript 2 corresponds to a higher density, $\rho_2 = \rho_{0a} z_2$, where $z_2 > z_1$, and a finite temperature T_2, with the corresponding values of the specific internal energy and pressure given by Eqs. (5) and (6), respectively. We write down the Hugoniot relation (1.71) of Ref. [45] in the form

$$\varepsilon_2(z_2, T_2) - \varepsilon_c(z_1) = \left(\frac{1}{z_1} - \frac{1}{z_2} \right) \frac{p_2(z_2, T_2) + p_c(z_1)}{2\rho_{0a}}. \quad (16)$$

For a given value of z_2, Eq. (16) is a quadratic equation in T_2. In this equation, the coefficient at T_2^2 is equal to

$$\frac{1}{2} \beta_0 z_2^{-\Gamma_e} - \frac{1}{2} \left(\frac{1}{z_1} - \frac{1}{z_2} \right) \frac{\Gamma_e}{2} \beta_0 z_2^{1-\Gamma_e}$$

$$= \frac{\Gamma_e}{4} \beta_0 z_2^{-\Gamma_e} \left(1 + \frac{2}{\Gamma_e} - \frac{z_2}{z_1} \right). \quad (17)$$

This coefficient is positive for the density compression parameter z_2/z_1 below the strong-shock limiting value of the density compression, $R_C = 1 + 2/\Gamma_e$, which for our choice of $\Gamma_e = 2/3$ equals 4. When $z_2/z_1 \to 4$, the temperature jump $T_2 \to \infty$, as should occur in the strong-shock limit. The free

term in the quadratic Hugoniot equation (16) is negative,

$$\varepsilon_c(z_2) - \varepsilon_c(z_1) - \left(\frac{1}{z_1} - \frac{1}{z_2} \right)$$

$$\times \frac{p_c(z_2) + p_c(z_1)}{2\rho_{0a}} < 0 \quad \text{at} \quad z_2 > z_1 \geqslant 1, \quad (18)$$

which is easily checked with the aid of Eqs. (10), (11). Therefore, for any z_2 in the interval $z_1 < z_2 < 4z_1$, Eq. (16) has one positive solution for T_2. Having evaluated this solution, we find the postshock density, temperature, and pressure. The shock velocity with respect to the preshock material, D, is then found from Eq. (1.67) of [45], which we write down in our notation as

$$D = \sqrt{\frac{\rho_2(p_2 - p_1)}{\rho_1(\rho_2 - \rho_1)}} = \sqrt{\frac{z_2(p_2 - p_1)}{z_1(z_2 - z_1)\rho_{0a}}}. \quad (19)$$

Figure 1 shows the Al (b) and Cu (c) Hugoniot curves that start on the $T = 0$ isotherm-isentrope from the initial density $\rho_1 = \rho_{0a}$ (the principal Hugoniot curve), and from the densities greater than that by a factor of 1.1, 1.2, and 1.4. Also shown are the experimental data for the principal Hugoniots of Al (b) and Cu (c) from Refs. [62,72,73]. Note that some of the Al data from Ref. [73] are taken at a cryogenic initial temperature 20 K, but this has not noticeably shifted the Hugoniot data from those taken at room temperature. The agreement between the above analytic formulas and the experimental data in the shock pressure range up to 4 Mbar is reasonable. It can be significantly improved by using more advanced approximations of the cold and thermal terms found in Refs. [65,66,68,70,71]. We will not be pursuing this for the reasons explained above.

It must be emphasized that although all the Hugoniot curves shown in Figs. 1(b), 1(c) start from the $T = 0$ isotherm-isentrope, the "Cold" curve, the corresponding shock strengths are all finite, even for the principal Hugoniot curves that start from the origin, where both $T = 0$ and $p = 0$. Indeed, as explained in [45], for low and moderate shock strengths, the cold contribution dominates in the postshock pressure; see Figs. 1(b), 1(c), where the principal Hugoniot curves plotted for $\rho_1 = \rho_{0a}$ closely follow the corresponding "Cold" curves in the low-pressure range. The density-dependent cold pressure makes a qualitative difference between the EOS of condensed materials and of an ideal gas. For the latter case, there is no cold pressure, the $T = 0$ isotherm-isentrope is also the $p = 0$ isobar, and any finite-pressure shock starting from this curve can be regarded as infinitely strong, compressing the preshock gas by the same factor of $R_C = (\gamma + 1)/(\gamma - 1)$. When the EOS accounts for the cold energy and pressure, the density and pressure buildup in the converging fluid is inconsistent with the assumption of uniform inflow velocity, $u = \text{constant} = u_0$. This is why self-similar Noh solutions based on this assumption do not exist for cylindrical and spherical geometry [13].

IV. SELF-SIMILAR SOLUTIONS OF THE NOH PROBLEM FOR CYLINDRICAL AND SPHERICAL GEOMETRY

We solve the ideal 1D compressible hydrodynamic equations. The equation of continuity is

$$\frac{\partial \rho}{\partial t} + u\frac{\partial \rho}{\partial r} + \frac{\rho}{r^{m-1}}\frac{\partial}{\partial r}(r^{m-1}u) = 0, \qquad (20)$$

where u is the radial velocity. We write down the Euler equation for the adiabatically compressed preshock material in the form

$$\frac{\partial u}{\partial t} + u\frac{\partial u}{\partial r} + \frac{K(\rho)}{\rho^2}\frac{\partial \rho}{\partial r} = 0, \qquad (21)$$

where the derivative in the definition of the adiabatic bulk modulus $K = \rho(\partial p/\partial \rho)_S$ is taken along the isentrope. For the isentrope corresponding to the initial state, the dependence $K(\rho)$ is a known function of density. Here we limit ourselves to the zero-temperature preshock isotherm-isentrope; hence, in our examples, $p = p_c(\rho)$, the dependence given by Eq. (10).

The problem formulation outlined in Sec. II is identical to the classic Noh case. At $t = 0^-$, an infinite space is filled with a material whose density and pressure are uniform. The initial velocity has the same absolute value u_0 everywhere, and it is directed at each point to the axis or center of symmetry in the cases of cylindrical and spherical symmetry, respectively. The material behind the accretion shock front expanding at a constant speed is at rest, and its density and pressure profiles are flat. We need to determine the preshock profiles of density, pressure, and velocity, calculate the strength of the expanding shock wave, and find the postshock density and pressure. For the examples presented below, the temperature and pressure of the uniform material at $t = 0^-$ are zero, and the density equals ρ_{0a}; see Sec. III and Table I. This choice of parameters is explained only by the convenience of expressing the density dependence of the adiabatic bulk modulus along the isentrope with the aid of (9). The existence of the self-similar solutions sought does not depend on this choice.

Solution of the above problem is self-similar. We denote the constant velocity of the expanding accretion shock front in the laboratory frame by u_s and introduce the self-similar coordinate η by

$$\eta = \frac{r}{u_s t}, \qquad (22)$$

so that the value of $\eta = 1$ refers to the expanding shock front, whereas $\eta > 1$ corresponds to the converging cold material ahead of it. The velocity and density of the converging cold material are sought in the form

$$u(r, t) = u_s \eta U(\eta), \qquad (23)$$

$$\rho(r, t) = \rho_{0a} N(\eta). \qquad (24)$$

Note that at $t \to 0^+$ we have $\eta \to \infty$ for each fluid particle at a finite distance from the axis or center of symmetry. Hence the above initial conditions translate into the following boundary conditions at infinity for the dimensionless profile functions $U(\eta)$ and $N(\eta)$:

$$\lim_{\eta \to \infty}(\eta U) = -u_0/u_s, \qquad (25)$$

$$\lim_{\eta \to \infty} N = 1. \qquad (26)$$

The continuity equation (20) translates into

$$\frac{(U-1)}{N}\eta\frac{dN}{d\eta} + \eta\frac{dU}{d\eta} + mU = 0. \qquad (27)$$

The Euler equation (21) with the aid of Eq. (9) is reduced to

$$(U-1)\left(\eta\frac{dU}{d\eta} + U\right) + \frac{K_{0a}(aN-1)^4}{\rho_{0a}u_s^2(a-1)^4\eta N^{13/3}}\frac{dN}{d\eta} = 0. \qquad (28)$$

The density-dependent adiabatic bulk modulus factor in the last term on the left-hand side of Eq. (28) is the only term in the system (27), (28) that accounts for a particular choice of EOS. The choice of the initial point on the cold isotherm-isentrope, $T = 0$, ensures that the density-dependent adiabatic bulk modulus is found with the aid of Eq. (9) where one substitutes $z = N$. A different choice of an EOS, or of the isentrope corresponding to the initial state, would only mean that the function $K(\rho)$ characteristic of this isentrope in (21) will be different.

For each material, there is a one-parameter family of the self-similar Noh solutions in cylindrical ($m = 2$) and spherical ($m = 3$) geometry. The most convenient parameter is the dimensional value of the expanding shock velocity, u_s. Having specified a value of u_s, we evaluate the dimensionless coefficient, $K_{0a}/\rho_{0a}u_s^2$, in Eq. (28). Then we can perform a numerical integration of Eqs. (27), (28) starting from the shock front, $\eta = 1$, to $\eta \to \infty$. Note that the initial conditions for the normalized density, $N(1^+) = N_1 > 1$, and the normalized velocity, $U(1^+) = U_1 < 0$, of the adiabatically compressed material entering the expanding accretion shock front are not known in advance. Rather, these constants have to be determined in the process of finding the numerical solution of the Noh problem.

The velocity of the adiabatically compressed material entering the shock front equals $u_s[\eta U(\eta)]_{\eta=1} = u_s U_1$, whereas the velocity of the shock front equals u_s. Therefore the velocity of the shock front with respect to the material entering it equals $D = u_s(1 - U_1)$. On the other hand, the shocked material near the axis or center of symmetry is assumed to be at rest, and therefore its velocity with respect to the expanding shock front equals u_s. The continuity equation implies that the parameter U_1 determines the shock density compression ratio:

$$\frac{N_2}{N_1} = \frac{z_2}{z_1} = 1 - U_1. \qquad (29)$$

We also require that the initial state of the material at $t = 0^+$, or, which is the same, at $\eta \to \infty$, corresponds to a zero pressure at the $T = 0$ isotherm-isentrope, which is expressed by the boundary condition (26). For a given trial value of U_1, we can determine the corresponding value of the normalized density $N_1 = z_1$ of the adiabatically compressed, finite-pressure cold material ahead of the shock front, at $\eta = 1^+$, from the requirement that the numerical solution asymptotically satisfies (26). This is easily done using a simple shooting method. By our assumption, the postshock normalized density is $N_2 = z_2 = z_1(1 - U_1)$. Substituting these values of z_1 and z_2 into the Hugoniot equation (16) and solving it as described in Sec. III, we calculate the shock velocity D from Eq. (19) and compare
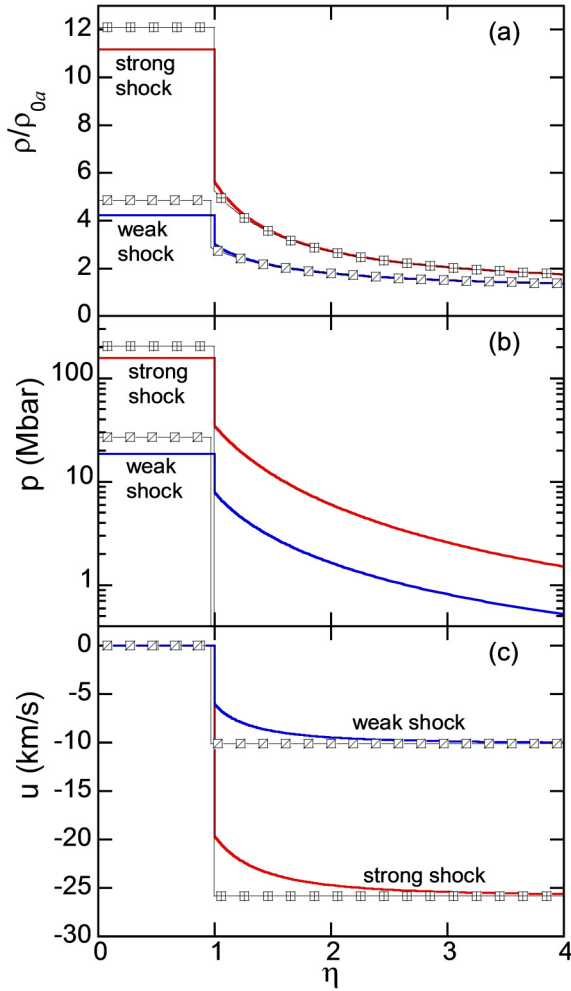
FIG. 2. Self-similar profiles of density compression (a), pressure (b), and radial velocity (c) for solutions of the spherical Noh problem for Al. Shock parameters for each case are listed in Table I. Lines with box symbols represent the constant-velocity approximate solution: the density profile is given by Eq. (31), the preshock pressure is zero, and the preshock velocity is equal to $-u_0$.
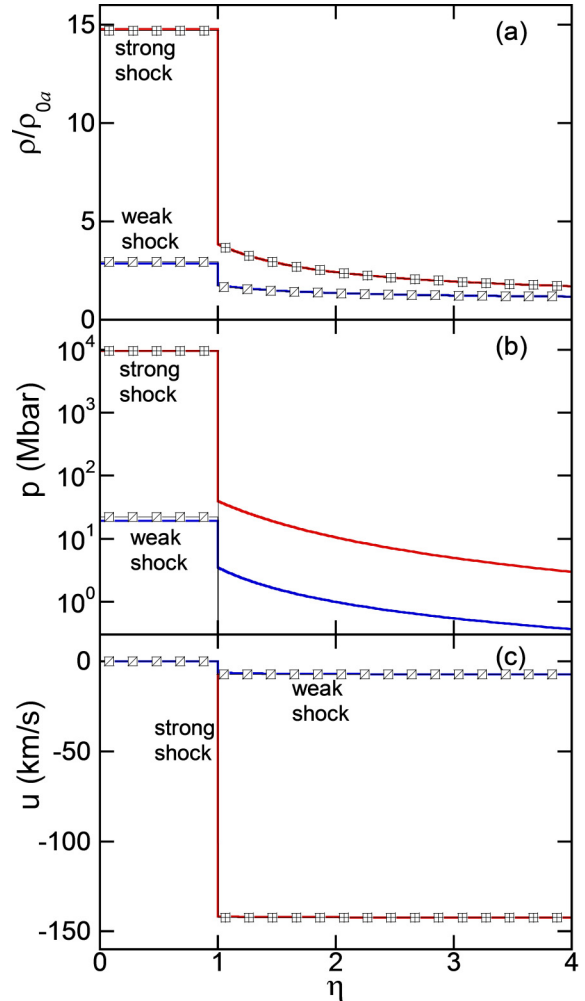

FIG. 3. Self-similar profiles of density compression (a), pressure (b), and radial velocity (c) for solutions of the cylindrical Noh problem for Cu. Shock parameters for each case are listed in Table I. Lines with box symbols represent the constant-velocity approximate solution: the density profile is given by Eq. (31), the preshock pressure is zero, and the preshock velocity is equal to $-u_0$.

this result with our trial value, $u_s(1 - U_1)$. The trial parameter U_1 is then chosen from the requirement that both expressions yield the same value for the shock velocity D. Having satisfied this requirement, we link the preshock solution of Eqs. (27), (28) via the Hugoniot jump conditions determined by our EOS with the postshock state of the uniform resting material behind the expanding accretion shock front. This completes the construction of the generalized Noh solution sought.

Figure 2 illustrates the self-similar profiles of density (a), pressure (b), and velocity (c) for solutions of the Noh problem in spherical geometry for aluminum. Figure 3 shows the same in cylindrical geometry for copper. Parameters of these solutions, as well as those for two cylindrical-geometry solutions for Al, are listed in Table I. For each combination of material and geometry, we present two examples, which are arbitrarily selected from the corresponding one-parametric families of solutions. The lower- and higher-intensity shock waves are labeled "weak" and "strong," respectively, although all of these shock waves produce Mbar-range pressure jumps.

Table I demonstrates, however, that the density compression ratios even in the strongest of these shocks are well below the value of $R_C = 4$ calculated for our model EOS in the strong-shock limit. The only example for which the adiabatic- and shock-compression parameters are formally within the range of applicability of the EOS model used here is the cylindrical "weak" shock solution for aluminum.

All the self-similar profiles shown in Figs. 2 and 3 are qualitatively alike. The adiabatic density compression due to the convergence produces a negative gradient of the cold pressure, which, in turn, slows down the incident material. Therefore the shock velocity with respect to the preshock material, D, is less than the sum of the shock velocity in the laboratory frame, u_s, and the incident velocity at infinity, u_0; see Table I. The relative difference between D and $u_s + u_0$ is understandably higher in a spherical geometry because a spherical convergence involves a faster density and pressure buildup than a cylindrical convergence. This difference is also

smaller for stronger shocks; it vanishes in the strong-shock limit of Ref. [47].

To elucidate the transition to this limit, we note that for large values of $u_s \to \infty$ the dimensionless factor $K_{0a}/\rho_{0a} u_s^2$ in the Euler equation (28) becomes small. Neglecting it in the first approximation, we find that the solution of Eq. (28) corresponds to a constant velocity, $U \propto 1/\eta$. Recalling that in this case $R_C = D/u_s = 1 + u_0/u_s$, and using the boundary condition (25), we find the approximate solution for the self-similar velocity:

$$U(\eta) = -\frac{R_C - 1}{\eta}. \tag{30}$$

Substituting (30) into (27), we can integrate this equation with the boundary condition (26) to obtain

$$N(\eta) = \left(1 + \frac{R_C - 1}{\eta}\right)^{m-1}, \tag{31}$$

which reproduces the classic Noh solution (2), as should occur. One can select a dimensionless value of R_C between 1 and 4 as a parameter determining a particular approximate solution of the Noh problem for a given material and convergence geometry. Substituting $z_1 = R_C^{m-1}$, $z_2 = R_C^m$ into the Hugoniot equation (16), we determine T_2 and thereby p_2. The shock velocity D is then found from Eq. (19), the velocities u_0 and u_s from Eq. (3). This is almost the same solution of the Noh problem as described in Ref. [47]. The difference is that the shock density compression ratio is not necessarily close to the Mie-Grüneisen strong-shock limiting value of $R_C = 1 + 2/\Gamma_2$, where Γ_2 is the postshock value of the Grüneisen coefficient (7) at $z = z_2 = R_C^m$, cf. Eq. (114) of Ref. [47], or to our strong-shock limiting value $R_C = 1 + 2/\Gamma_e = 4$ determined by the constant electronic Grüneisen coefficient $\Gamma_e = 2/3$. Rather, it has to be found from the Hugoniot equations for a finite shock strength. Choosing the value of R_C to make the convergence velocity u_0 in the approximate solution the same as in the computed semianalytic solution (evaluated numerically as described above), we can compare the approximate solution of the Noh problem outlined above with the numerically accurate one for the same initial conditions.

The approximate solutions for the spherical and cylindrical geometry are shown in Figs. 2 and 3, respectively, as lines with box symbols. It turns out that the above approximation is fairly accurate in predicting the velocity u_s of the expanding shock front in the laboratory frame in all cases. For example, its deviation from the exact value is less than 3% and 1% for the weak-shock and strong-shock spherical solutions for Al shown in Fig. 2. For the same cases, the density compression ratios are 21% and 16% off, and postshock pressures 44% and 30% off, respectively, as shown in Fig. 2. This is not surprising because the approximate solution that neglects the preshock velocity decrease requires a larger velocity jump at the shock front to stop the incident flow, implying a stronger shock wave. A good agreement for the spherical geometry is only achieved in the Gbar shock pressure range.

On the other hand, for cylindrical geometry the preshock velocity decrease is lower, which makes the constant-velocity approximation more accurate. It is hard to see the difference between the lines representing the density and velocity profiles given by the exact and approximate solutions for Cu in Fig. 3. Even for the weak-shock case, the values of the velocity u_s, compression ratio R_C, and postshock pressure p_s given by the approximate solution are off only by 0.7%, 7%, and 15%, respectively.

We have shown that, with condensed materials, the explicit solutions [47] for the cylindrical and spherical Noh problem, which do not exactly satisfy Eqs. (20), (21), can reasonably approximate self-similar solutions of these equations. The accuracy of this approximation is determined, for our model EOS, by the smallness of the parameter $K_{0a}/\rho_{0a} u_s^2$ characteristic of the relative values of cold and ram pressures, and by the geometry of convergence.

V. CONCLUSIONS

We have presented semianalytic self-similar solutions of the Noh problem in cylindrical and spherical geometry for a simple model EOS that approximates cold- and shock-compression properties of condensed materials with a reasonable accuracy. The EOS used here does not satisfy the symmetry constraints [46,47] that make it possible to derive self-similar solutions of the blast-wave [46,53], converging-shock [54,55,59], or impulsive-loading [45,56,57] problems for materials with non-ideal-gas equations of state.

The generalized, semianalytic, self-similar solutions of the Noh problem and the classic ones [1] are qualitatively very much alike. The difference is that the expanding accretion shock wave has a finite strength, and the preshock adiabatic density compression results in a pressure buildup, which, in turn, slows down the converging preshock material. The self-similar solutions are not given by explicit formulas, as in the classic case [1]. Rather, they need to be numerically calculated using the simple procedure described above. In contrast to the classic case of Ref. [1] or the strong-shock limit of Ref. [47], the solutions have to be constructed for specific values of material parameters and finite shock strength. From the derivation of our examples in Sec. IV it is clear that other, different self-similar solutions of the Noh problem can be likewise constructed for other materials and different EOS models. As in the case of an ideal-gas EOS, the existence of the self-similar solutions does not require the initial temperature and/or pressure of the converging material to be zero.

The self-similar solutions of the Noh problem for an arbitrary EOS exist because, when the initial density, pressure, and velocity profiles are flat, the scales of all the flow variables in our problem do not depend on time. In other words, the initial and boundary conditions of the problem contain a characteristic velocity u_0, and characteristic values of the density and pressure, but no parameters from which a characteristic length or time scale can be constructed. Therefore the solution of the problem has to be self-similar, i.e., depending on the coordinate r and time t only via a dimensional combination like $r/u_s t$. In this respect, too, the Noh problem stands out among the other fundamental 1D problems of ideal compressible fluid dynamics permitting self-similar solutions, such as the blast-wave problem [46,53], the converging-shock problem [54,55,59], or the impulsive-loading problem [45,56,57]. All these other problems involve shock waves whose strength changes as they propagate. Hence the self-similarity of their

solutions is not consistent with finite shock strength, i.e., with a time dependence of the shock density compression ratio. This constraint does not exist only for the Noh problem, where the accretion shock strength does not change as it propagates, and therefore it can be finite and essentially arbitrary. So can be the EOS of the converging material.

We have chosen to use the simplest analytical EOS model compatible with the decomposition (5), (6). The purpose of this work is to present some examples and to explain how the self-similar solutions of the Noh problem can be constructed for an EOS that accounts for the cold energy and pressure and, therefore, does not satisfy the symmetry constraints of Refs. [46,47]. To construct a solution as described above, one only needs an expression for the adiabatic bulk modulus as a function of density along the chosen isentrope, and expressions for the specific internal energy and pressure making it possible to calculate, for given parameters of the preshock state and a trial value of the shock density compression ratio, the full set of the postshock parameters including the shock velocity D with respect to the material entering it. Obviously, this information can be obtained for any analytical EOS model, resulting in EOS- and material-specific Noh solutions. One can even consider the materials with "anomalous" thermodynamic properties, whose nonconvex EOSs allow for rarefaction shocks; see Chap. I, Sec. 19, and Chap. XI, Sec. 20, of [45],

as well as [74,75]. The generalized Noh solutions can be used for verification of hydrocodes with all kinds of non-ideal-gas EOSs in one dimension.

The solutions also provide a convenient platform for accretion-shock stability studies in a cylindrical and spherical geometry. Like the classic Noh solutions, the solutions here include a resting core of a uniform shocked material surrounding the axis or center of symmetry. Therefore a linear stability analysis of such solutions would result in explicit dispersion equations, similar to that derived for the classic case in Ref. [40]. Stability study, in this case, is much easier than the analysis required to describe the small-amplitude RM instability [38] in materials that do not satisfy the stability criterion [44] for reflected and/or transmitted shock front(s). The simplest analytical non-ideal-gas EOS that satisfies the DK instability criteria is the van der Waals EOS [76]. This EOS can be presented in the form (5), (6), and therefore, it can be readily used for constructing generalized Noh solutions as described above. When this work is done, the results of such analysis will be available for hydrocode verification in two and three dimensions, in both stable and DK-unstable parameter ranges.

[1] W. F. Noh, Errors for calculations of strong shocks using artificial viscosity and an artificial heat flux, J. Comput. Phys. **72**, 78 (1987).

[2] K. Wu, Accretion onto magnetic white dwarfs, Space Sci. Rev. **93**, 611 (2000).

[3] H.-Th. Janka, Explosion mechanisms of core-collapse supernovae, Annu. Rev. Nucl. Part. Sci. **62**, 407 (2012).

[4] S. V. Lebedev, F. N. Beg, S. N. Bland, J. P. Chittenden, A. E. Dangor, M. G. Haines, K. H. Kwek, S. A. Pikuz, and T. A. Shelkovenko, Effect of discrete wires on the implosion dynamics of wire array Z pinches, Phys. Plasmas **8**, 3734 (2001); S. V. Lebedev, F. N. Beg, S. N. Bland, J. P. Chittenden, A. E. Dangor, and M. G. Haines, Snowplow-like behavior in the implosion phase of wire array Z pinches, *ibid.* **9**, 2293 (2002).

[5] S. C. Bott, D. M. Haas, Y. Eshaq, U. Ueda, F. N. Beg, D. A. Hammer, B. Kusse, J. Greenly, T. A. Shelkovenko, S. A. Pikuz, I. C. Blesener, R. D. McBride, J. D. Douglass, K. Bell, P. Knapp, J. P. Chittenden, S. V. Lebedev, S. N. Bland, G. N. Hall, F. A. Suzuki Vidal, A. Marocchino, A. Harvey-Thomson, M. G. Haines, J. B. A. Palmer, A. Esaulov, and D. J. Ampleford, Study of the effect of current rise time on the formation of the precursor column in cylindrical wire array Z pinches at 1 MA, Phys. Plasmas **16**, 072701 (2009).

[6] E. P. Yu, A. L. Velikovich, and Y. Maron, Application of one-dimensional stagnation solutions to three-dimensional simulation of compact wire array in absence of radiation, Phys. Plasmas **21**, 082703 (2014).

[7] Y. Maron, A. Starobinets, V. I. Fisher, E. Kroupp, D. Osin, A. Fisher, C. Deeney, C. A. Coverdale, P. D. LePell, E. P. Yu, C. Jennings, M. E. Cuneo, M. C. Herrmann, J. L. Porter, T. A. Mehlhorn, and J. P. Apruzese, Pressure and Energy Balance of Stagnating Plasmas in *z*-Pinch Experiments: Implications

to Current Flow at Stagnation, Phys. Rev. Lett. **111**, 035001 (2013).

[8] C. A. Coverdale, C. Deeney, A. L. Velikovich, R. W. Clark, Y. K. Chong, J. Davis, J. Chittenden, C. L. Ruiz, G. W. Cooper, A. J. Nelson, J. Franklin, P. D. LePell, J. P. Apruzese, J. Levine, J. Banister, and N. Qi, Neutron production and implosion characteristics of a deuterium gas-puff Z pinch, Phys. Plasmas **14**, 022706 (2007); C. A. Coverdale, C. Deeney, A. L. Velikovich, J. Davis, R. W. Clark, Y. K. Chong, J. Chittenden, S. Chantrenne, C. L. Ruiz, G. W. Cooper, A. J. Nelson, J. Franklin, P. D. LePell, J. P. Apruzese, J. Levine, and J. Banister, Deuterium gas-puff Z-pinch implosions on the Z accelerator, *ibid.* **14**, 056309 (2007).

[9] M. Gehmeyr, B. Cheng, and D. Mihalas, Noh's constant-velocity shock problem revisited, Shock Waves **7**, 255 (1997).

[10] A. L. Velikovich, J. L. Giuliani, S. T. Zalesak, J. W. Thornhill, and T. A. Gardiner, Exact self-similar solutions for the magnetized Noh Z pinch problem, Phys. Plasmas **19**, 012707 (2012).

[11] H. Azechi, T. Sakaiya, T. Watari, M. Karasik, H. Saito, K. Ohtani, K. Takeda, H. Hosoda, H. Shiraga, M. Nakai, K. Shigemori, S. Fujioka, M. Murakami, H. Nagatomo, T. Johzaki, J. Gardner, D. G. Colombant, J. W. Bates, A. L. Velikovich, Y. Aglitskiy, J. Weaver, S. Obenschain, S. Eliezer, R. Kodama, T. Norimatsu, H. Fujita, K. Mima, and H. Kan, Experimental Evidence of Impact Ignition: 100-Fold Increase of Neutron Yield by Impactor Collision, Phys. Rev. Lett. **102**, 235002 (2009).

[12] R. A. Agnew, J. T. Cassibry, and B. H. Winterling, Analytic model to estimate thermonuclear neutron yield in Z-pinches using the magnetic Noh problem, IEEE Trans. Plasma Sci. **44**, 2181 (2016).

[13] S. D. Ramsey, Z. M. Boyd, and S. C. Burnett, Solution of the Noh problem using the universal symmetry of the gas dynamics equations, Shock Waves **27**, 477 (2017).

[14] J. U. Brackbill, D. B. Kothe, and H. M. Ruppel, FLIP: A low-dissipation, particle-in-cell method for fluid-flow, Comput. Phys. Commun. **48**, 25 (1988).

[15] M. Shashkov and B. Wendroff, A composite scheme for gas dynamics in Lagrangian coordinates, J. Comput. Phys. **150**, 502 (1999).

[16] S.-H. Bae and R. T. Lahey, Jr., On the use of nonlinear filtering, artificial viscosity, and artificial heat transfer for strong shock computations, J. Comput. Phys. **153**, 575 (1999).

[17] W. J. Rider, Revisiting wall heating, J. Comput. Phys. **162**, 395 (2000).

[18] L. D. G. Sigalotti, H. López, A. Donoso, E. Sira, and J. Klapp, A shock-capturing SPH scheme based on adaptive kernel estimation, J. Comput. Phys. **212**, 124 (2006).

[19] M. Omang, S. Børve, and J. Trulsen, SPH in spherical and cylindrical coordinates, J. Comput. Phys. **213**, 391 (2006).

[20] R. C. Batra and G. M. Zhang, Modified smoothed particle hydrodynamics (MSPH) basis functions for meshless methods, and their application to axisymmetric Taylor impact test, J. Comput. Phys. **227**, 1962 (2008).

[21] E. Johnsen, J. Larsson, A. V. Bhagatwala, W. H. Cabot, P. Moin, B. J. Olson, P. S. Rawat, S. K. Shankar, B. Sjögreen, H. C. Yee, X. Zhong, and S. K. Lele, Assessment of high-resolution methods for numerical simulations of compressible turbulence with shock waves, J. Comput. Phys. **229**, 1213 (2010).

[22] G. Scovazzi, J. N. Shadid, E. Love, and W. J. Rider, A conservative nodal variational multiscale method for Lagrangian shock hydrodynamics, Comput. Methods Appl. Mech. Eng. **199**, 3059 (2010).

[23] K. Lipnikov and M. Shashkov, A framework for developing a mimetic tensor artificial viscosity for Lagrangian hydrocodes on arbitrary polygonal meshes, J. Comput. Phys. **229**, 7911 (2010).

[24] R. Loubère, P.-H. Maire, and P. Váchal, 3D staggered Lagrangian hydrodynamics scheme with cell-centered Riemann solver-based artificial viscosity, Int. J. Numer. Meth. Fl. **72**, 22 (2013).

[25] I. Sagert, W. Bauer, D. Colbry, J. Howell, R. Pickett, A. Staber, and T. Strother, Hydrodynamic shock wave studies within a kinetic Monte Carlo approach, J. Comput. Phys. **266**, 191 (2014).

[26] S. Hickel, C. P. Egerer, and J. Larsson, Subgrid-scale modeling for implicit large eddy simulation of compressible flows and shock-turbulence interaction, Phys. Fluids **26**, 106101 (2014).

[27] X. Hu, S. Jiang, and R. Wang, A MUSCL smoothed particles hydrodynamics for compressible multi-material flows, Math. Method. Appl. Sci. **39**, 1093 (2016).

[28] D. Fridrich, R. Liska, and B. Wendroff, Some cell-centered Lagrangian Lax-Wendroff HLL hybrid schemes, J. Comput. Phys. **326**, 878 (2016).

[29] R. M. Cabezón, D. García-Senz, and J. Figueira, SPHYNX: An accurate density-based SPH method for astrophysical applications, Astron. Astrophys. **606**, A78 (2017).

[30] D. Linga, J. Cheng, and C.-W. Shu, Positivity-preserving and symmetry-preserving Lagrangian schemes for compressible Euler equations in cylindrical coordinates, Comput. Fluids **157**, 112 (2017).

[31] L. Taddei, N. Lebaal, and S. Roth, Axis-symmetrical Riemann problem solved with standard SPH method: Development of a polar formulation with artificial viscosity, Comput. Math. Appl. **74**, 3161 (2017).

[32] S.-J. Paardekooper, Multidimensional upwind hydrodynamics on unstructured meshes using graphics processing units. I. Two-dimensional uniform meshes, Mon. Not. R. Astron. Soc. **469**, 4306 (2017).

[33] D. E. Burton, N. R. Morgan, M. R. J. Charest, M. A. Kenamond, and J. Fung, Compatible, energy conserving, bounds preserving remap of hydrodynamic fields for an extended ALE scheme, J. Comput. Phys. **355**, 492 (2018).

[34] X. Liu, N. R. Morgan, and D. E. Burton, A Lagrangian discontinuous Galerkin hydrodynamic method, Comput. Fluids **163**, 68 (2018).

[35] V. Dobrev, Tz. Kolev, D. Kuzmin, R. Rieben, and V. Tomov, Sequential limiting in continuous and discontinuous Galerkin methods for the Euler equations, J. Comput. Phys. **356**, 372 (2018).

[36] R. D. Richtmyer, Taylor instability in shock acceleration of compressible fluids, Commun. Pure Appl. Math. **13**, 297 (1960).

[37] E. E. Meshkov, Instability of the interface of two gases accelerated by a shock wave. Sov. Fluid Dyn. **4**, 101 (1969).

[38] M. Brouillette, The Richtmyer-Meshkov instability, Annu. Rev. Fluid Mech. **34**, 445 (2002).

[39] Y. Zhou, Rayleigh-Taylor and Richtmyer-Meshkov instability induced flow, turbulence, and mixing. Part I, Phys. Rep. **720-722**, 1 (2017); Rayleigh-Taylor and Richtmyer-Meshkov instability induced flow, turbulence, and mixing. Part II, **723-725**, 1 (2017).

[40] A. L. Velikovich, M. Murakami, B. D. Taylor, J. L. Giuliani, S. T. Zalesak, and Y. Iwamoto, Stability of stagnation via an expanding accretion shock wave, Phys. Plasmas **23**, 052706 (2016).

[41] A. L. Velikovich, Analytic theory of Richtmyer-Meshkov instability for the case of reflected rarefaction wave, Phys. Fluids **8**, 1666 (1996).

[42] S. P. D'yakov, On the stability of shock waves, Zh. Eksp. Teor. Fiz. **27**, 288 (1954) (in Russian).

[43] V. M. Kontorovich, Concerning the stability of shock waves, Sov. Phys. JETP **6**, 1179 (1958).

[44] L. D. Landau and E. M. Lifshitz, *Fluid Mechanics* (Pergamon Press, Oxford, 1987).

[45] Ya. B. Zel'dovich and Yu. P. Raizer, *Physics of Shock Waves and High-Temperature Hydrodynamic Phenomena*, 2nd ed. (Dover, New York, 2002).

[46] L. I. Sedov, *Similarity and Dimensional Methods in Mechanics*, 10th ed. (CRC Press, Boca Raton, 1993).

[47] R. A. Axford, Solutions of the Noh problem for various equations of state using Lie groups, Laser Part. Beams **18**, 93 (2000).

[48] G. M. Ward and D. I. Pullin, A study of planar Richtmyer-Meshkov instability in fluids with Mie-Grüneisen equations of state, Phys. Fluids **23**, 076101 (2011).

[49] J. G. Wouchuk and J. López Cavada, Spontaneous acoustic emission of a corrugated shock wave in the presence of a reflecting surface, Phys. Rev. E **70**, 046303 (2004).

[50] J. W. Bates, Theory of the corrugation instability of a piston-driven shock wave, Phys. Rev. E **91**, 013014 (2015).

[51] A. M. Molodets, Generalized Grüneisen function for condensed media, Combust., Explos. Shock Waves (Engl. Transl.) **31**, 620 (1995).

[52] A. M. Molodets, Grüneisen function and the zero-temperature isotherm of three metals up to pressures of 10 TPa, JETP **80**, 467 (1995).

[53] L. I. Sedov, Le mouvement d'air en cas d'une forte explo-

sion, Compt. Rend. (Dokl.) Acad. Sci. URSS **52**, 17 (1946) (in French); G. Taylor, The formation of a blast wave by a very intense explosion. I. Theoretical discussion, Proc. R. Soc. London, Ser. A **201**, 159 (1950); J. von Neumann, The point source solution, in H. A. Bethe, K. Fuchs, J. O. Hirschfelder, J. L. Magee, R. E. Peierls, and J. von Neumann, Blast wave, Los Alamos Scientific Laboratory Report LA-2000, written in 1947, distributed in 1958, pp. 27–55.

[54] G. Guderley, Starke kugelige und zylindrische Verdichtungsstöße in der Nähe des Kugelmittelpunktes bzw. der Zylinderachse, Luftfahrtforschung **19**, 302 (1942) (in German).

[55] K. P. Stanyukovich, *Unsteady Motion of Continuous Media* (Academic Press, New York, 1960).

[56] S. von Hoerner, Lösungen der hydrodynamischen Gleichungen mit linearem Verlauf der Geschwindigkeit, Z. Naturforsch. A **10a**, 687 (1955) (in German); W. Häfele, Zur analytishen Behandlung ebener, starker, instationärer Stoßwellen, *ibid.* **10a**, 1006 (1955) (in German); V. B. Adamskii, Integration of a system of self-similar equations in the problem of an impulsive load on cold gas, Sov. Phys. Acoust. **2**, 1 (1956); Ya. B. Zel'dovich, Motion of a gas under the action of an impulsive pressure (load), *ibid.* **2**, 25 (1956); A. I. Zhukov and Ya. M. Kazhdan, On the motion of a gas under the action of a short duration impulse, *ibid.* **2**, 375 (1956).

[57] S. I. Anisimov and V. A. Kravchenko, Shock wave in condensed matter generated by impulsive load, Z. Naturforsch. **40a**, 8 (1985).

[58] C. C. Wu and P. H. Roberts, Structure and stability of a spherical shock wave in a van der Waals gas, Q. J. Mech. Appl. Math. **49**, 501 (1996).

[59] S. D. Ramsey, E. M. Schmidt, Z. M. Boyd, J. F. Lilieholm, and R. S. Baty, Converging shock flows for a Mie-Grüneisen equation of state, Phys. Fluids **30**, 046101 (2018).

[60] V. N. Zharkov and V. A. Kalinin, *Equations of State for Solids at High Pressures and Temperatures* (Consultants Bureau, New York, 1971).

[61] S. C. Burnett, D. G. Sheppard, K. G. Honnell, and T. Sjostrom, Sesame-style decomposition of KS-DFT molecular dynamics for direct interrogation of nuclear models, in *Shock Compression of Condensed Matter 2017* (AIP, to be published), arXiv:1708.09380.

[62] L. V. Al'tshuler, S. B. Kormer, A. A. Bakanova, and R. F. Trunin, Equation of state for aluminum, copper, and lead in the high pressure region, Sov. Phys. JETP **11**, 573 (1960).

[63] I. C. Slater, *Introduction in the Chemical Physics* (McGraw Book Co., New York, 1935).

[64] L. D. Landau and K. P. Stanyukovich, On a study of the detonation of condensed explosives, Compt. Rend. (Dokl.) Acad. Sci. URSS **46**, 362 (1945).

[65] A. M. Molodets, Equation of state for solid chemical elements, Dokl. Phys. **42**, 173 (1997).

[66] E. I. Kraus and I. I. Shabalin, A few-parameter equation of state of the condensed matter, J. Phys.: Conf. Ser. **774**, 012009 (2016).

[67] J. S. Dugdale and D. K. MacDonald, The thermal expansion of solids, Phys. Rev. **89**, 832 (1953).

[68] A. F. Nikiforov, V. G. Novikov, and V. B. Uvarov, *Quantum-Statistical Models for Hot Dense Matter: Methods for Computation Opacity and Equation of State* (Birkhäuser, Berlin, 2005).

[69] R. F. Trunin, Shock compressibility of condensed materials in strong shock waves generated by underground nuclear explosions, Phys. Usp. **37**, 1123 (1994).

[70] D. A. Liberman, Self-consistent field model for condensed matter, Phys. Rev. B **20**, 4981 (1979).

[71] B. G. Wilson, V. Sonnad, P. Sterne, and W. Isaacs, PURGATORIO: A new implementation of the INFERNO algorithm, J. Quant. Spectrosc. Radiat. Transfer **99**, 658 (2006).

[72] A. C. Mitchell and W. J. Nellis, Shock compression of aluminum, copper, and tantalum, J. Appl. Phys. **52**, 3363 (1981).

[73] M. D. Knudson, R. W. Lemke, D. B. Hayes, C. A. Hall, C. Deeney, and J. R. Asay, Near-absolute Hugoniot measurements in aluminum to 500 GPa using a magnetically accelerated flyer plate technique, J. Appl. Phys. **94**, 4420 (2003).

[74] A. G. Ivanov and S. A. Novikov, Rarefaction shock waves in iron and steel, Sov. Phys. JETP **13**, 1321 (1961).

[75] A. A. Borisov, Al. A. Borisov, S. S. Kutateladze, and V. E. Nakoryakov, Rarefaction shock wave near the critical liquid-vapour point, J. Fluid Mech. **126**, 59 (1983).

[76] J. W. Bates and D. C. Montgomery, The D'yakov-Kontorovich Instability of Shock Waves in Real Gases, Phys. Rev. Lett. **84**, 1180 (2000).